DACOMAT

Deliverable number: D1.3

Determining the governing factors for promotion of secondary delamination fronts

Stergios Goutianos

DTU

The DACOMAT project has received funding from the European Union's Horizon 2020 research and innovation programme under GA No. 761072

Deliverable details

Document name: D1.3 Determining the governing factors for promotion of secondary delamination fronts

Responsible partner: Technical University of Denmark (DTU)

Work package: WP1

Task: 1.2

Due date: 31-12-2019

Delivery date: 23-12-2019

Dissemination level	
x	PU = Public
	CO = Confidential, only for members of the consortium (including the EC)
	Classified, information as referred to in Commission Decision 2001/844/EC.
Deliverable type	
x	R: Document, report (excluding the periodic and final reports)
	DEM: Demonstrator, pilot, prototype, plan designs
	DEC: Websites, patents filing, press & media actions, videos, etc.
	OTHER: Software, technical diagram, etc.

The DACOMAT project has received funding from the European Union's Horizon 2020 research and innovation programme under GA No. 761072

Popular science summary

Composite materials can fail in delamination in a pseudo-ductile manner e.g. deformation (large crack opening) occurs before separation. This is a desired feature in designing structures. There is, however, a need to increase the fracture resistance of composite materials as structures such as wind turbine blades become longer and longer. Large structures has a higher possibility of defects that can lead to delaminations and eventually to structural failure. An increase in fracture resistance can be achieved by modifying the constituent materials or by promoting failure mechanisms that increase the fracture resistance. An interesting approach to increase fracture resistance is to promote close parallel cracks. The presence of multiple cracks can lead to significantly higher resistance to fracture. However, for this failure mode to work positively, the characteristics of the cracks need to be controlled. The simplest case is two cracks. In this report we investigate which crack characteristics that provide the highest fracture resistance (for example crack strength or distance between the cracks). Since it would be quite time consuming to perform this investigation experimentally, we use numerical modelling.

The DACOMAT project has received funding from the European Union's Horizon 2020 research and innovation programme under GA No. 761072

Contents

The DACOMAT project has received funding from the European Union's Horizon 2020 research and innovation programme under GA No. 761072

1. Summary

In this report, the governing factors for promotion of secondary delamination (parallel to the primary delamination) fronts are investigated using cohesive zone based finite element modelling. First, the literature is summarised, and the motivation is given. Then, the applied cohesive laws are briefly described. The finite element details follow. Finally, the results are presented with several examples. Based on the results, in the conclusion recommendation are given on how to use the mechanism of parallel delaminations to obtain the maximum possible increase in fracture resistance. The main finding is that the formation of the secondary crack is controlled by the peak tractions the main and the secondary crack. Even when the two parallel cracks are far apart, a maximum in fracture resistance can be achieved if the peak tractions of the two parallel cracks are carefully controlled.

The DACOMAT project has received funding from the European Union's Horizon 2020 research and innovation programme under GA No. 761072

2. Background

A target of the DACOMAT project is to significantly increase the fracture resistance of composite materials using the concept of multiple parallel cracks. The benefit of this approach is schematically illustrated in Figure 1. The crack growth rate, under cyclic loading, is constant for a crack without fibre bridging. Fibre bridging results in a lower crack growth rate and in the presence of multiple cracks, the crack growth under cyclic loading may even stop (crack arrest).

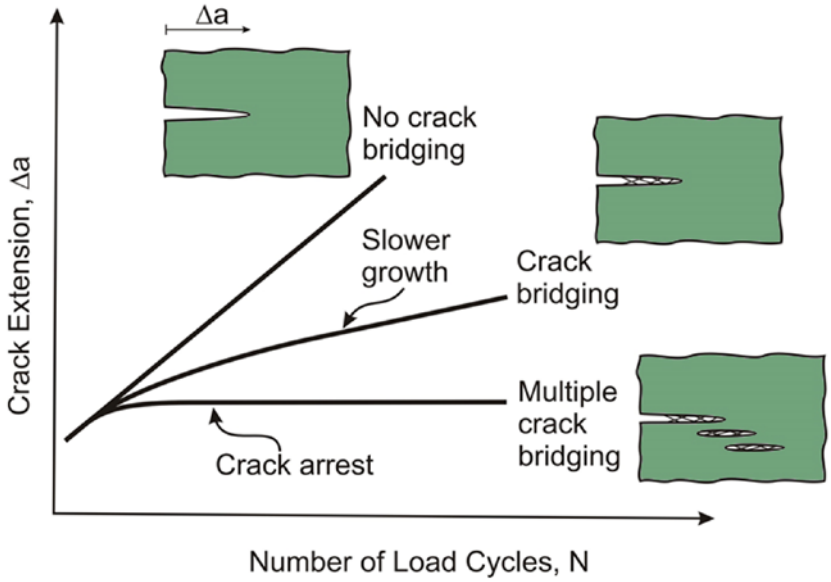

Figure 1 Schematic illustration of crack extension rate with the number of loading cycles for a crack without fibre bridging, for a crack with fibre bridging and for the case of multiple parallel cracks with fibre bridging.

2.1 Motivation

The approach of increasing the fracture resistance by multiple parallel cracks was motivated by the experimental data of Rask & Sørensen, 2012. They tested Double Cantilever Beam (DCB) specimens andobserved that by changing the lay-up of glass fibre/polyester composite beams bonded together with a thermoset adhesive, parallel delaminations developed as shown in Figure 2.

The corresponding fracture resistance curves for one, two and three delaminations (or parallel cracks) are shown in Figure 3. As i can be seen, the steady-state fracture resistance increases approximately proportionally with the number of secondary cracks (cracks parallel to the primary or initial crack). Based on this observation, a linear relationship may exist between the number of cracks (or fracture process zones) and the overall steady-state fracture resistance.

Similar results, a significant increase of the steady-state fracture resistance was observed in the experimental work of Kusano, Sørensen, & Andersen, 2013 as shown in Figure 4.

2.2 Analytical modelling

Goutianos & Sørensen, 2016 developed an analytical model for two growing parallel cracks by applying the J-integral (Rice, 1968) to analyse the problem. The aim of the study was to investigate if the

The DACOMAT project has received funding from the European Union's Horizon 2020 research and innovation programme under GA No. 761072

experimental data from the previous sections represent a general mechanism to considerably increase the steady-state fracture resistance.

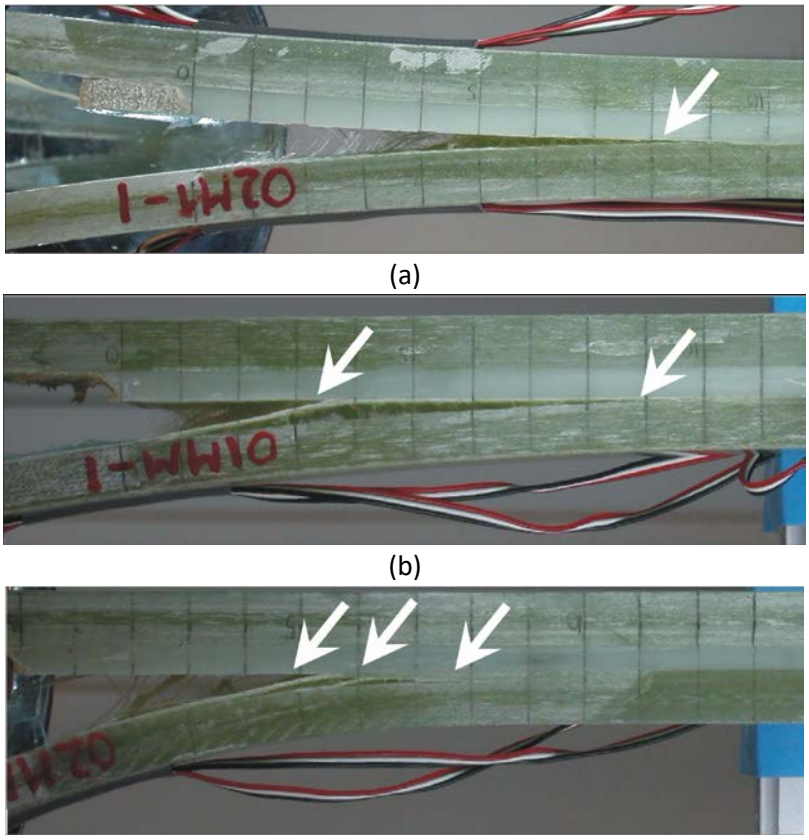

(a)

(b)

(c)

Figure 2 Photographs of Double Cantilever Beam (DCB) adhesive joint specimens loaded with pure bending moments: a) one crack, b) two and c) three cracks (Rask & Sørensen, 2012).

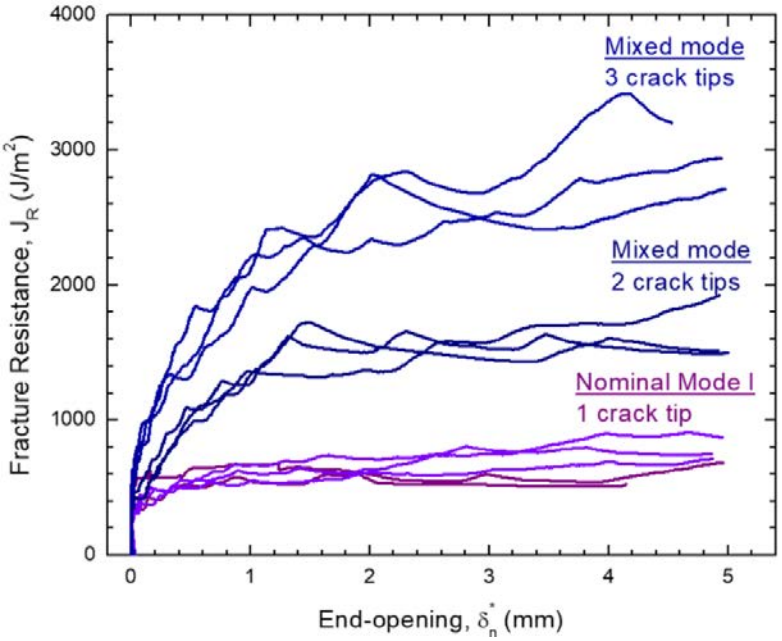

Figure 3 Fracture resistance curves as a function of the (normal) end-opening for DCB specimens with different number of delaminations / parallel cracks *(Rask & Sørensen, 2012)*.

The DACOMAT project has received funding from the European Union's Horizon 2020 research and innovation programme under GA No. 761072

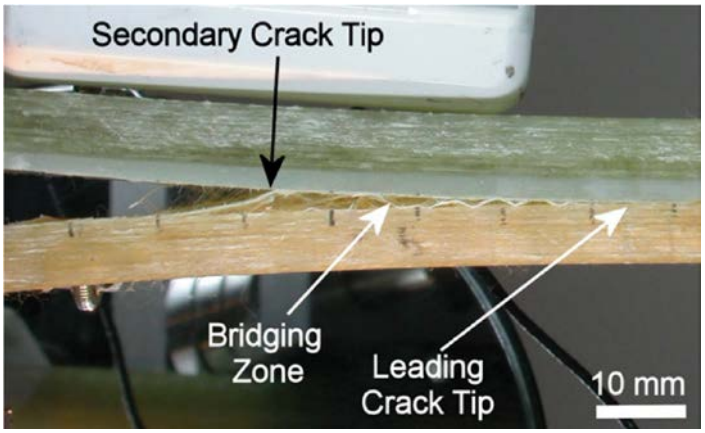

Figure 4 Formation of two parallel cracks: one inside the laminate and one at the laminate/adhesive interface in a DCB adhesive joint specimen *(Kusano., Sørensen, & Andersen, 2013)*.

The problem analysed is shown in Figure 5. To simplify the analysis, only two parallel cracks (primary and secondary cracks) were considered. In addition, it was assumed that both cracks open only in mode I. The local J-integral paths Γ_{loc} that encloses the two cracks is shown with a dashed line.

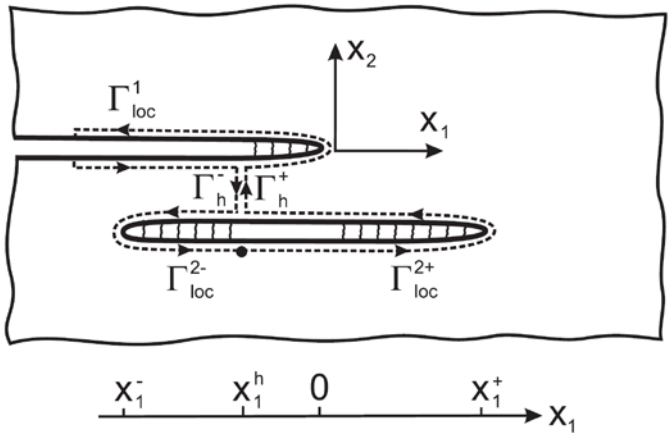

Figure 5 Local J-integral paths Γ_{loc} enclosing the primary crack, denoted as 1, and secondary crack, denoted as 2 (Goutianos & Sørensen, 2016).

It was shown that when the left crack tip of the secondary crack opens, the local J-integral is:

$$J_{loc} = J^1_{loc} = J^1_{n,ss} \quad (1)$$

That is the only contribution comes from the local J-integral that encloses the primary crack and thus the overall steady-state fracture resistance is equal to the steady-state fracture resistance of the primary crack.

When, the left crack tip of the secondary crack remains closed, then the overall steady-state fracture resistance is:

$$J_{loc} = J^1_{loc} + J^{2+}_{loc} = J^1_{n,ss} + J^2_{n,ss} \quad (2)$$

The DACOMAT project has received funding from the European Union's Horizon 2020 research and innovation programme under GA No. 761072

where $J^2_{n,ss}$ is the steady-state fracture resistance of the secondary crack. In this case there is a positive contribution to the overall steady-state fracture resistance from the right tip of the secondary crack.

Eq. 2 can be generalised to N parallel cracks:

$$J_{loc} = J^1_{n,ss} + N\, J^2_{n,ss} \qquad 3$$

Using Eq. *3*, the experimental results presented above can be theoretically explained. Eq. *1* gives the lower limit in the steady-state fracture resistance (the left crack tip of the secondary crack opens), whereas Eq. *3* gives the upper limit of the steady-state fracture resistance (when the left crack tip of the secondary crack remains closed). For more details the reader is referred to the work of (Goutianos & Sørensen, 2016). It should be noted that the analytical model can be generalised to mixed mode loading and it is not restricted only to the case of mode I.

2.3 Numerical modelling

Goutianos & Sørensen, 2016 valiadated the analytical model, briefly presented above, with a numerical model (cohesive zone modelling in a finite element framework). They have used a Double Cantilever Beam specimen loaded with pure bending moments (see Figure 6). The aim was mainly to investigate if and to which extent the left crack tip of the secondary crack tip opens. This is not possible with the analytical model, which considers only two cases: a closed and an opened right crack tip. It should be noted that both the analytical and numerical models are valid for large-scale fracture process zones similar to the facture process zone observed in the composite materials developed in the DACOMAT project.

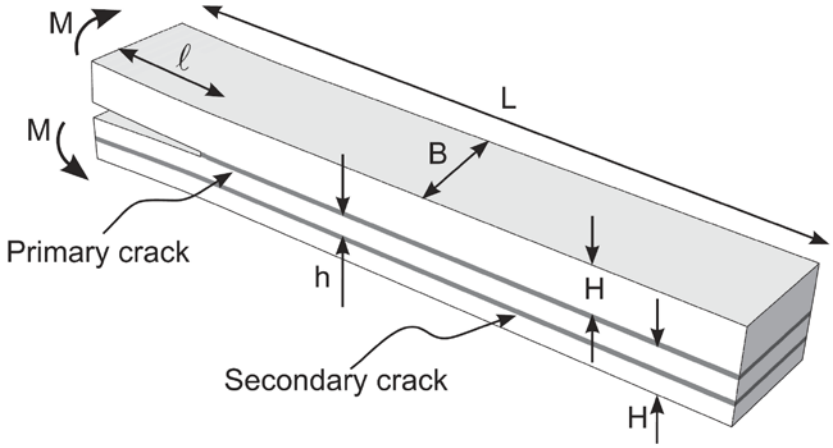

Figure 6 Double Cantilever Beam (DCB) specimen subjected to pure bending moments, M. Two cohesive zones, at a distance h, where modelled allowing the initiation and growth of two parallel cracks (Goutianos & Sørensen, 2016).

Within the cohesive zone, the material behaviour is described by a cohesive law or traction-separation law. A schematic illustration of a cohesive law is shown in Figure 7 (for mode I and mode II). The mode I peak traction is denoted as $\hat{\sigma}^i_n$ where $i = 1$ for the primary crack and $i = 2$ for the secondary crack. The peak traction defines when damage initiates in the cohesive zone (crack initiation). Once damage has initiated, the traction decreases and finally drops to zero when the opening reaches the critical value, $\delta^{c,i}_n$. The area under the traction-separation curve equals the fracture energy. For example for mode I and the primary crack, the fracture energy is $J^1_{n,ss}$ (see Section 2.2).

The DACOMAT project has received funding from the European Union's Horizon 2020 research and innovation programme under GA No. 761072

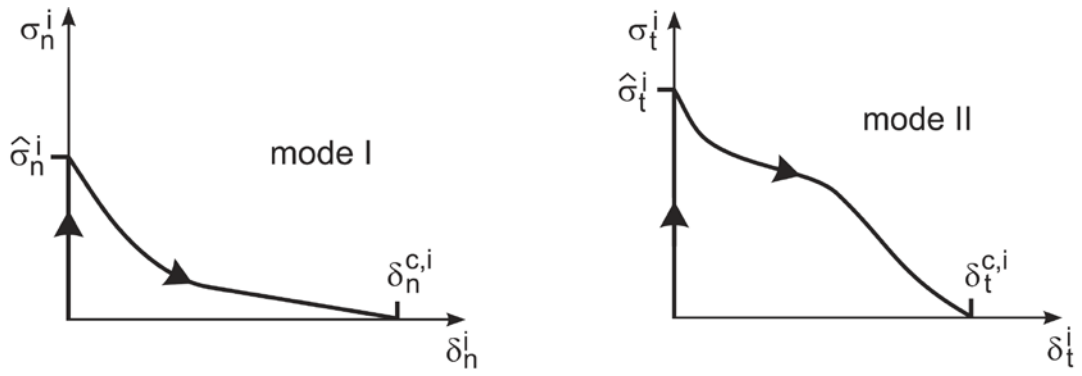

(a) (b)

Figure 7 Schematic illustration of mode I and mode II cohesive laws.

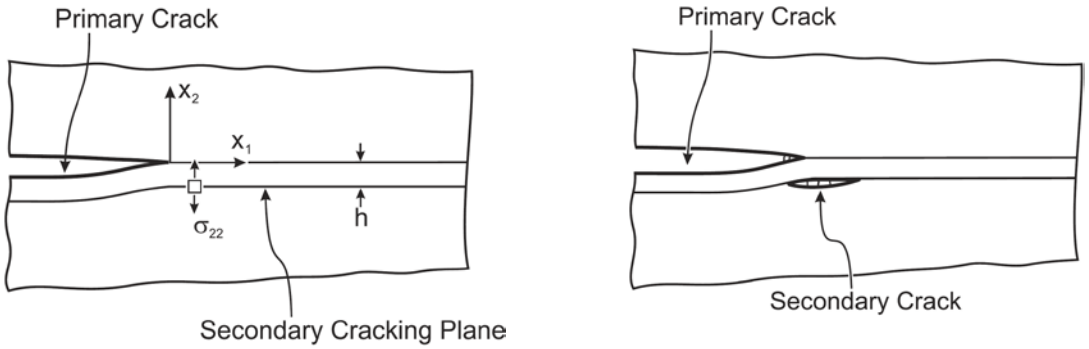

(a) (b)

Figure 8 Mechanism of the secondary crack formation.

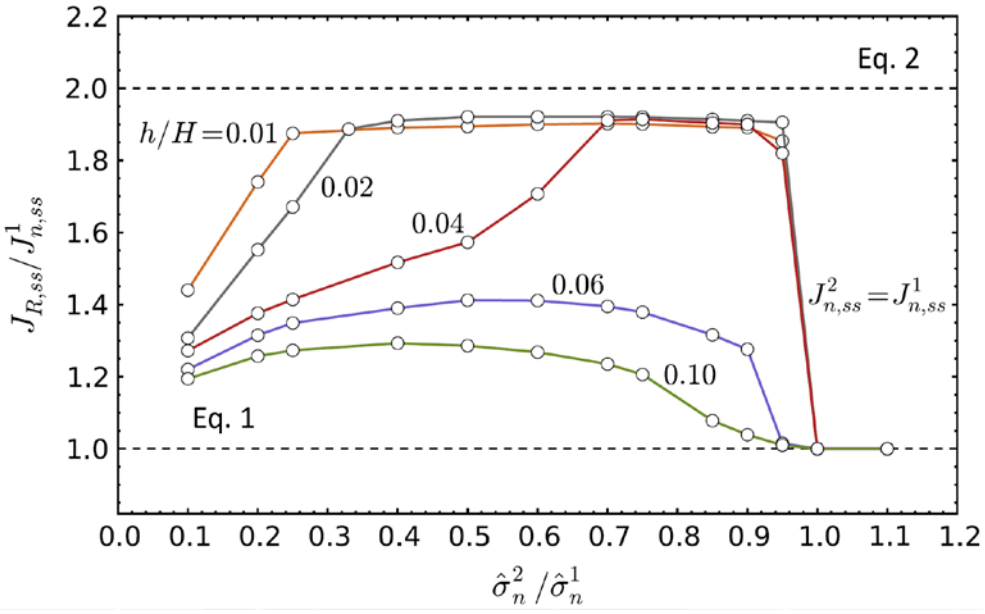

Figure 9 Steady-state fracture resistance, $J_{R,ss}$, as a function of the normal peak traction of the secondary crack, $\hat{\sigma}_n^2$. The fracture energy for the cohesive law of the secondary crack equals the fracture energy of the cohesive law for the primary crack. The mode II cohesive law is identical to the mode I cohesive law for both cracks (Goutianos & Sørensen, 2016).

The DACOMAT project has received funding from the European Union's Horizon 2020 research and innovation programme under GA No. 761072

Figure 8 shows the mechanism of the secondary crack formation. When the normal stress at the tip of the notch reaches the normal peak traction, the primary crack begins to open. If the normal stress, σ_{22}, in any material within the secondary cracking plane (cohesive zone) is lower than the normal peak traction no secondary crack will form. By further increasing the applied load, the fracture process zone of the primary crack evolves. If at any material point, within the secondary cracking plane, the normal stress reaches the normal peak traction of the secondary crack cohesive law, then a secondary crack is formed (Figure 8b).

Figure 9 shows the main findings of Goutianos & Sørensen, 2016. The steady-state fracture resistance, $J_{R,ss}$, approaches the upper limit (see Eq. 2) for a wide range of peak traction ratios, $\hat{\sigma}_n^2/\hat{\sigma}_n^1$, as long as the distance, h, between the cracking planes is relative small compared to the height, H, of the specimen. Thus, the concept of increasing the steady-state fracture resistance by introducing weak planes is feasible and robust. However, in many cases like composite laminates made out of relatively thick laminas, it is not possible to have the weak plane very close to the primary crack as the minimum distance is defined by the thickness of the lamina. In this case, there can be still a significant increase in steady-state fracture resistance as shown in Figure 9, but the increase is far from the maximum increase achievable with small *h*/*H* ratios .

The results presented in Figure 9 are based on cohesive laws with linear softening (see Section 3) and more importantly on a fixed ratio $\hat{\sigma}_n^1/E$ equal to $5.0e^{-5}$ where E is the Young's modulus of the composite in the fibre direction. In the present report, the parametric study is significantly more extensive compared to the work of Goutianos & Sørensen, 2016, in order to find the cohesive law parameters that result in maximum increase of the steady-state fracture resistance for all cases even when the two cracking planes are far apart. Secondly, a more realistic cohesive law is implemented which has two linear softening regions: one to describe the crack tip fracture process zone and one for the fibre bridging fracture process zone.

The DACOMAT project has received funding from the European Union's Horizon 2020 research and innovation programme under GA No. 761072

3. Cohesive law

In this Section of the cohesive laws used in the present report will be briefly described. Two cohesive laws were derived and then they were implemented as user material subroutines (VUMAT) for the Abaqus commercial finite element program. The subroutines were written in the Fortran programming language. The first cohesive law is a law with linear softening as in the work of Goutianos & Sørensen, 2016 but with several improvements such as more variables as output and available to the Abaqus graphical user interface. The second cohesive law is described by bi-linear softening in order to separate the cracktip fracture process zone and the fibre bridging fracture process zone.

3.1 Linear softening behaviour

Figure 10 shows the pure normal and tangential (shear) cohesive laws for the primary and secondary crack. Although the problem analysed (see Figure 6) is primarily a mode I problem, due to the asymmetry introduced by the secondary crack, there is a small mode II opening. Thus, the mode II component of the cohesive law is also modelled. For more details the reader is referred to the work of (Goutianos & Sørensen, 2016). Here only the main characteristics of the cohesive laws will be described. It is assumed that that normal and shear cohesive laws are fully uncoupled e.g. the normal traction, σ_n, depends only on the normal opening, δ_n, and the shear traction, σ_t, depends only on the shear opening, δ_t. The link between the mode I and mode II components is provided by a failure criterion:

$$F = \frac{W_n^i}{J_{n,ss}^i} + \frac{W_t^i}{J_{t,ss}^i} \qquad 4$$

where W_n^i is the normal work of tractions and W_t^i the shear work of tractions (shaded areas in Figure 10). The unloading is assumed linear as shown in Figure 10. The mixed mode cohesive law is potential-based and thus path independent.

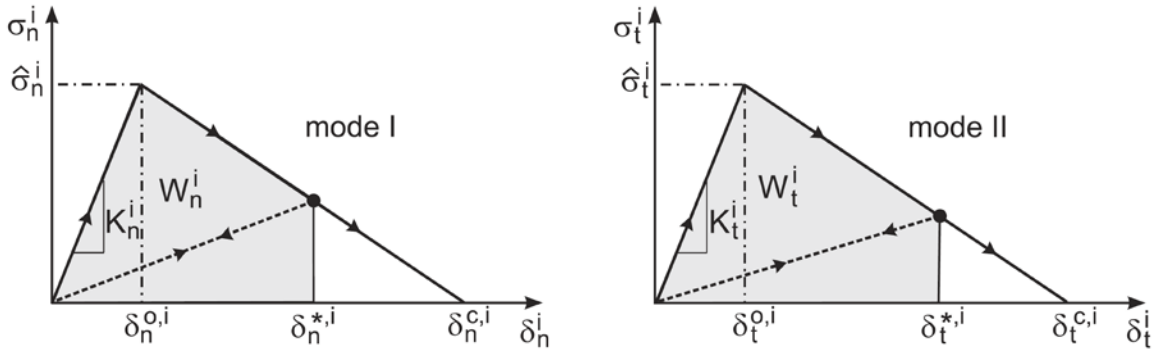

(a) (b)

Figure 10 Mode I and mode II linear softening cohesive laws for the primary ($i = 1$) and secondary crack ($i = 2$).

The non-dimensional parameters defining the problem are:

$$\begin{matrix} h/H & \hat{\sigma}_n^1/E & J_{n,ss}^1/(EH) \\ \hat{\sigma}_n^2/\hat{\sigma}_n^1 & \hat{\sigma}_t^1/\hat{\sigma}_n^1 & \hat{\sigma}_t^2/\hat{\sigma}_n^2 \\ J_{n,ss}^2/J_{n,ss}^1 & J_{t,ss}^1/J_{n,ss}^1 & J_{t,ss}^2/J_{n,ss}^2 \end{matrix} \qquad 5$$

The DACOMAT project has received funding from the European Union's Horizon 2020 research and innovation programme under GA No. 761072

3.2 Bi-linear softening behaviour

The advantage of the linear softening cohesive law (Section 3.1) is its simplicity and the relatively few parameters required for a full description. In practise, however, the cohesive law shape is more complex. Figure 11 shows the fully developed fracture process zone of a filament winded unidirectional glass fibre composite. The derived mode I cohesive law is shown in Figure 12. There is a crack tip fracture process zone characterised by a high peak traction (approximately 22 MPa) and small opening (less than 10 μm). At the wake of the crack tip, there is the fibre bridging fracture process zone. It is a large zone, characterised by small tractions (less than approximately 2 MPa) and large openings (up to 8 mm).

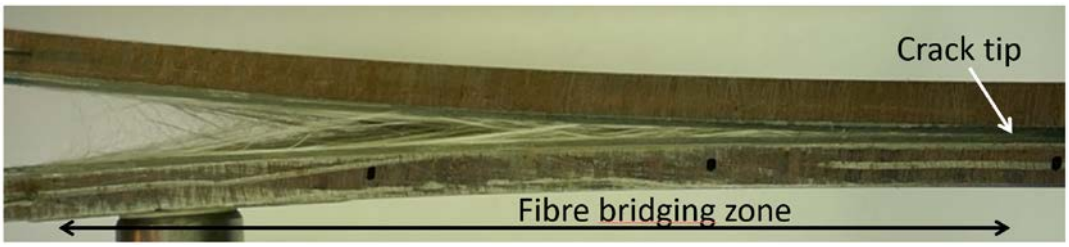

Figure 11 Fracture process zone in unidirectional composite material (DACOMAT Report D3.6).

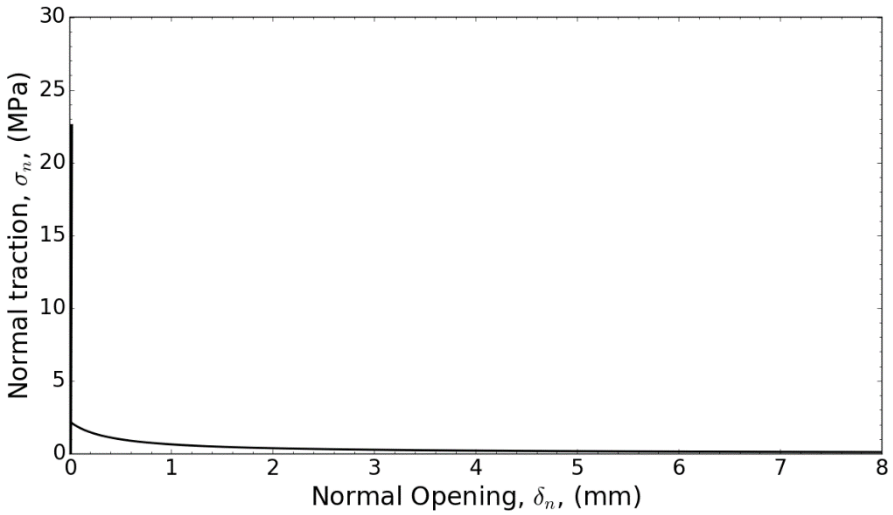

Figure 12 Mode I cohesive law for the specimen shown in Figure 11 (DACOMAT Report D3.6).

The cohesive law of Figure 12 can be approximated by a cohesive law with a bi-linear softening shape, schematically illustrated in Figure 13. In Figure 13, the mode I component for the primary crack is shown. The shape for the mode I cohesive law for the secondary crack is similar e.g. $1 \rightarrow 2$. The mode II components (for both cracks) also have the same shape with $n \rightarrow t$.

The same mixed mode failure criterion given by Eq. 4 is used. The work of tractions and fracture energies are given in Figure 13.

The DACOMAT project has received funding from the European Union's Horizon 2020 research and innovation programme under GA No. 761072

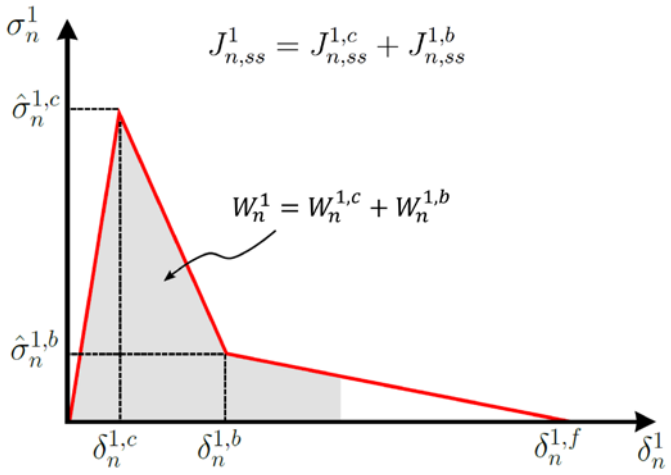

Figure 13 Mode I bi-linear softening cohesive law for the primary ($i = 1$). For the secondary crack $1 \rightarrow 2$, and for the mode II component $n \rightarrow t$. The symbol c refers to the crack tip, and b to the bridging zone.

It is clear from Figure 13, that the parameters needed to define the bi-linear softening cohesive law are significantly more numerous than those needed for the linear softening cohesive law. The following non-dimensional parameters fully describe the cohesive laws:

$$\begin{matrix} \hat{\sigma}_n^{1,b} / \hat{\sigma}_n^{1,c} & J_{n,ss}^{1,b} / J_{n,ss}^{1,c} \\ \hat{\sigma}_n^{2,b} / \hat{\sigma}_n^{2,c} & J_{n,ss}^{2,b} / J_{n,ss}^{2,c} \\ \hat{\sigma}_n^{2,c} / \hat{\sigma}_n^{1,c} & J_{n,ss}^{2,c} / J_{n,ss}^{1,c} \\ \hat{\sigma}_n^{2,b} / \hat{\sigma}_n^{1,b} & J_{n,ss}^{2,b} / J_{n,ss}^{1,b} \end{matrix} \qquad 6$$

and

$$\begin{matrix} \hat{\sigma}_t^{1,b} / \hat{\sigma}_t^{1,c} & J_{t,ss}^{1,b} / J_{t,ss}^{1,c} \\ \hat{\sigma}_t^{2,b} / \hat{\sigma}_t^{2,c} & J_{t,ss}^{2,b} / J_{t,ss}^{2,c} \\ \hat{\sigma}_t^{2,c} / \hat{\sigma}_t^{1,c} & J_{t,ss}^{2,c} / J_{t,ss}^{1,c} \\ \hat{\sigma}_t^{2,b} / \hat{\sigma}_t^{1,b} & J_{t,ss}^{2,b} / J_{t,ss}^{1,b} \end{matrix} \qquad 7$$

Two additional non-dimensional parameters are the distance between the two cracking planes:

$$h = H \qquad 8$$

the ratio:

$$\hat{\sigma}_n^{1,c} / E \qquad 9$$

and

$$J_{n,ss}^1 / (EH) \qquad 10$$

The DACOMAT project has received funding from the European Union's Horizon 2020 research and innovation programme under GA No. 761072

4. Finite element model

The crack growth problem of Figure 6 was modelled by the finite element method using the commercial FE-code Abaqus as a plane strain problem (see Figure 14). In Figure 14 the loads (prescribed rotations) and the boundary conditions can be seen.

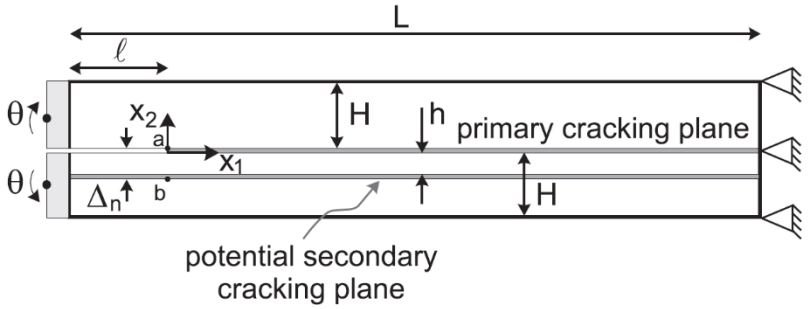

Figure 14 Geometry, loads and boundary conditions of the finite element model. The cracking planes (cohesive zones) where crack can initiate and grow are indicated.

For this specimen geometry and loading, the external J-integral (along the external boundaries of the specimen) is given by:

$$J_{ext} = (1-\nu)^2 \frac{21(M_1^2 + M_2^2) - 6\,M_1\,M_2}{4B^2H^3E} \qquad 11$$

Thus, the fracture resistance can be computed from the finite element simulations by first extracting the reactions moments (M_1 and M_2) and then applying Eq. 11.

It should be mentioned that convergence difficulties are commonly observed when modelling crack growth with implicit finite element methods. A number of numerical stability methods exist to overcome these difficulties, however an explicit FE method is more robust. In the present study, an explicit solver was used to solve the problem under quasi-static conditions using mass-scaling. In all simulations, it was ensured that the sum of the kinetic energy and the energy dissipated by viscosity (viscous damping is always included in Abaqus/Explicit) was less than 0.5% of the strain energy.

The DACOMAT project has received funding from the European Union's Horizon 2020 research and innovation programme under GA No. 761072

5. Results

As it can be seen from Eq. 5-10, an extensive parameter study is required for both cohesive laws and in particular for the cohesive law with bi-linear softening response. Therefore, only the most important results will be presented in this report.

5.1 Linear softening behaviour

Figure 15 shows the steady-state fracture resistance as a function of the peak traction of the secondary crack with respect to the peak traction of the primary crack when the two cracks are relatively far apart ($h/H = 0.1$). The results are plotted for three different ratios of $\hat{\sigma}_n^1/E$. The case $\hat{\sigma}_n^1/E = 5.0e^{-5}$ is replotted from Figure 9 where it was stated that for this case the increase of the steady-state fracture resistance was not maximum (closer to Eq. 1 which represents no positive effect from the secondary crack). It can be seen from Figure 15 that when $\hat{\sigma}_n^1$ increases, it is possible to achieve the maximum steady-state fracture resistance even when the two cracks are far apart. For $\hat{\sigma}_n^1/E = 5.0e^{-4}$ the steady-state fracture resistance is nearly two times the fracture resistance of a single crack. This result indicates that both peak tractions have to be modified when h/H is large. The peak traction of the primary crack must be increased, and the peak traction of the secondary crack should be between 0.2 to 0.4 $\hat{\sigma}_n^1$.

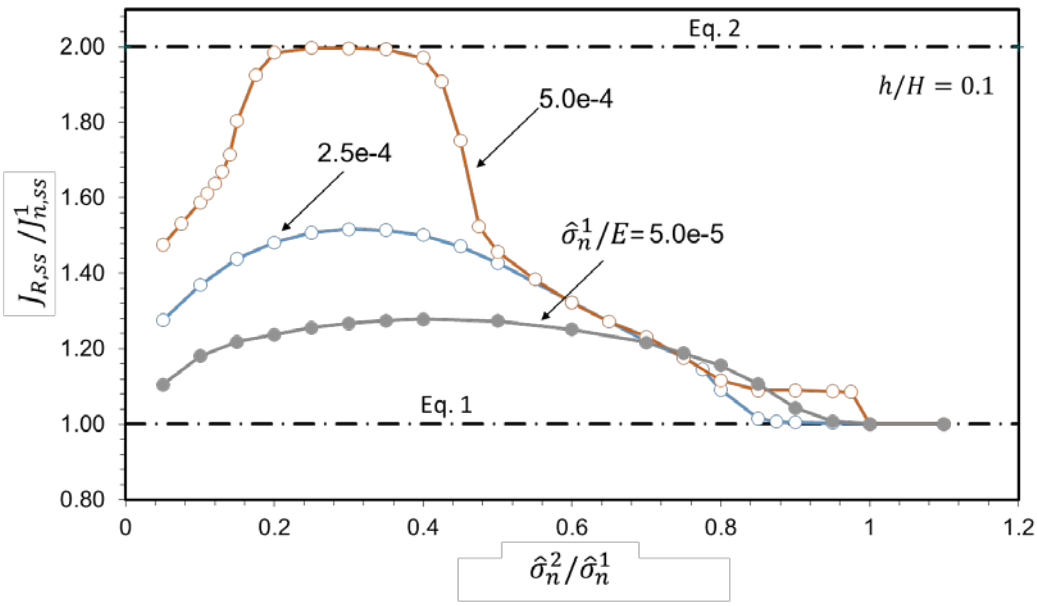

Figure 15 Steady-state fracture resistance, $J_{R,ss}$, as a function of the normal peak traction of the secondary crack, $\hat{\sigma}_n^2$, for three different $\hat{\sigma}_n^1/E$ ratios. The distance between the two cracks is $h/H = 0.1$. The fracture energy for the cohesive law of the secondary crack equals the fracture energy of the cohesive law for the primary crack. The mode II cohesive law is identical to the mode I cohesive law for both cracks. The cohesive laws have a linear softening behaviour.

In Figure 15 the fracture energy of the secondary crack is equal to the fracture energy of the primary crack. In Figure 16, the effect of varying the fracture energy of the secondary crack is investigated for two peak traction ratios and $\hat{\sigma}_n^1/E = 5e^{-4}$. When the fracture energy of the secondary crack is smaller than the fracture energy of the primary crack, it can be seen that the steady-state fracture resistance is approximately equal to the upper limit of the analytical model. Further increase of the fracture

The DACOMAT project has received funding from the European Union's Horizon 2020 research and innovation programme under GA No. 761072

energy of the secondary crack results in a deviation from the upper limit. The same trend is observed in Figure 17 where $\hat{\sigma}_n^1/E$ is equal to $\hat{\sigma}_n^1/E = 1e^{-3}$.

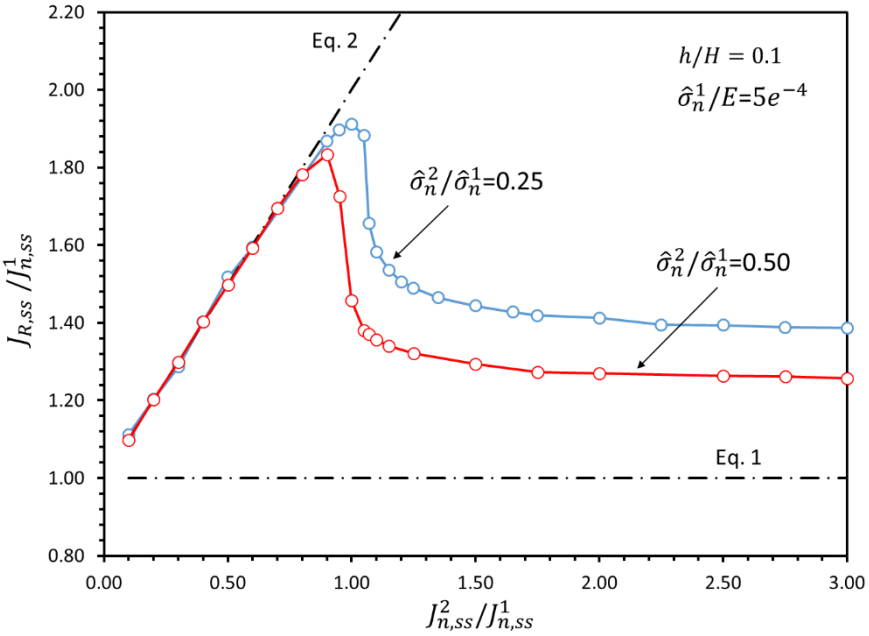

Figure 16 Steady-state fracture resistance, $J_{R,ss}$, as a function of the mode I fracture energy of the secondary crack for two peak traction ratios $\hat{\sigma}_n^2/\hat{\sigma}_n^1$. The distance between the two cracks is $h/H = 0.1$, $\hat{\sigma}_n^1/E = 5e^{-4}$. For both cracks, the mode II cohesive law is identical to the corresponding mode I cohesive law.

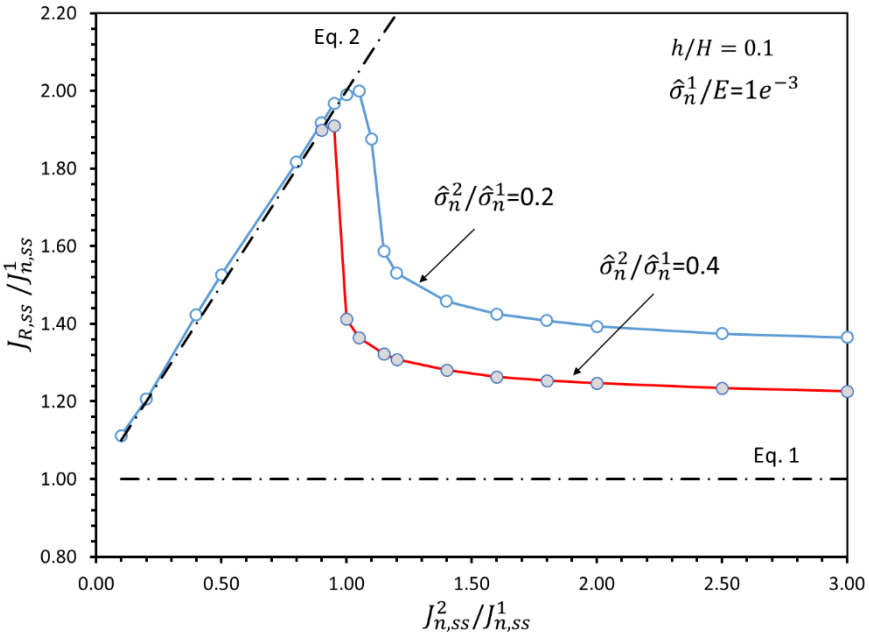

Figure 17 Steady-state fracture resistance, $J_{R,ss}$, as a function of the mode I fracture energy of the secondary crack for two peak traction ratios $\hat{\sigma}_n^2/\hat{\sigma}_n^1$. The distance between the two cracks is $h/H = 0.1$, $\hat{\sigma}_n^1/E = 1e^{-3}$. For both cracks, the mode II cohesive law is identical to the corresponding mode I cohesive law.

The DACOMAT project has received funding from the European Union's Horizon 2020 research and innovation programme under GA No. 761072

In Figure 18 the steady-state fracture resistance is plotted when the fracture energy of both cracks increases (as $J^1_{n,ss}$ increases, $\delta_n^{c,1}$increases). When the fracture energy of both cracks is small, it can be seen that the steady-state fracture resistance is equal to the maximum possible fracture resistance. When the fracture energies increase, the steady-state fracture resistance deviates from the upper limit and approaches the lower limit. However, the total steady-state fracture resistance is higher.

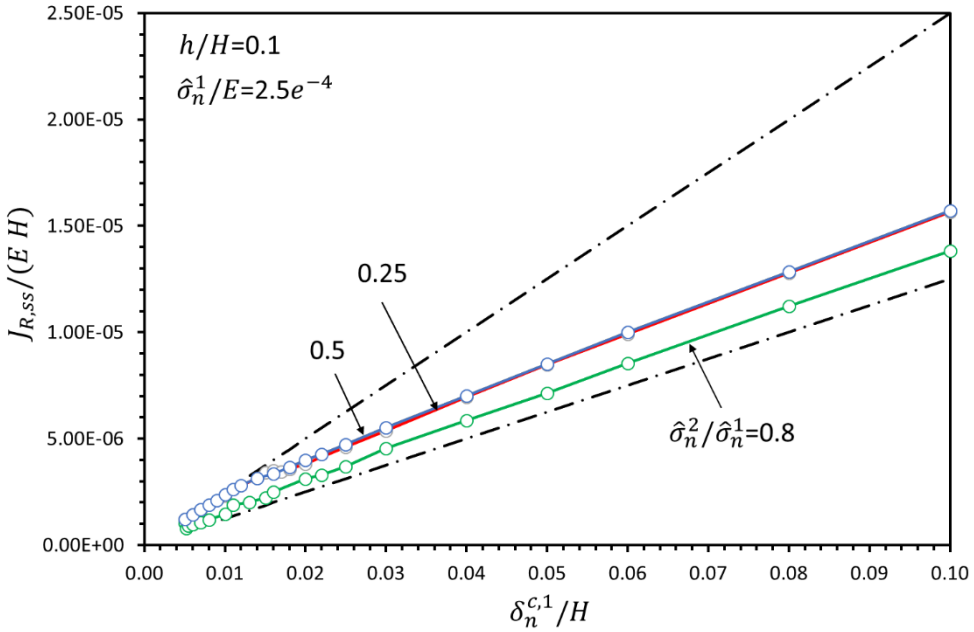

Figure 18 Steady-state fracture resistance as a function of the critical opening of the primary crack for different peak traction ratios $\hat{\sigma}_n^2/\hat{\sigma}_n^1$. The primary cohesive law has the same mode I fracture energy with the secondary cohesive law. The mode II fracture energy equals the mode I fracture energy for both cohesive laws.

5.2 Detailed investigation of the analytical model

In Figure 19 - Figure 21, the analytical model of Section 2.2 is examined in detail. The focus is mainly to examine the outcome of the analytical model with regards to the issue that the left crack tip of the secondary crack has a negative contribution to the fracture resistance if it opens.

In the results presented above, the fracture resistance is calculated from Eq. 11 e.g. based on the J-integral along the external boundaries of the DCB specimen. In Figure 19 the fracture resistance, J_{ext}, is plotted as function of the combined end-opening of the primary and secondary cracks for a certain set of parameters for the two cracks. In the same plot, the work of tractions, W_{total}, is plotted. W_{total} is calculated by post-processing the finite element results and it is the sum of normal and shear tractions of both cracks. As expected, $J_{ext} = W_{total}$ for the entire crack growth history up to steady-state.

In Figure 20 the contribution form the normal tractions of the primary crack (W_n^1) and from the left crack tip (W_n^{2-}) and right crack tip (W_n^{2+}) of the secondary crack are plotted. Initially there is a strong negative contribution from the left crack tip. This contribution decreases as the crack approaches the steady-state and is close to zero at steady-state and thus the overall steady-state fracture resistance

The DACOMAT project has received funding from the European Union's Horizon 2020 research and innovation programme under GA No. 761072

is nearly equal to the upper limit in accordance to Eq. 2. At this point the left crack tip is closed as verified by visualizing the deformed shape of the finite element solution.

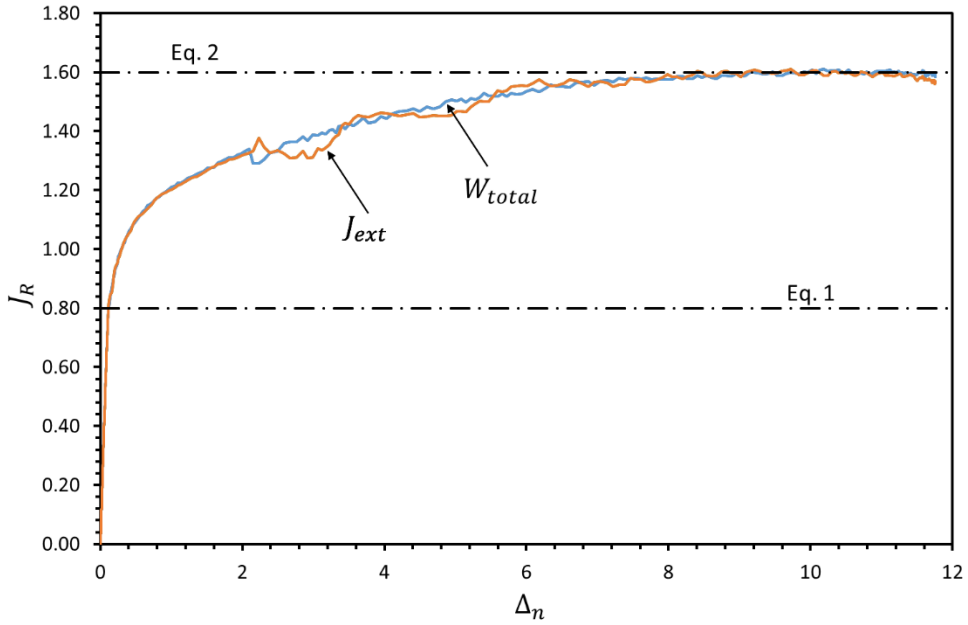

Figure 19 Fracture resistance as a function of the normal end-opening (of both the primary and secondary crack). J_{ext} is calculated from Eq. 11. W_{total} is the work of all tractions. $\hat{\sigma}_n^1/E = 5.0e^{-4}$, $\hat{\sigma}_n^2/\hat{\sigma}_n^1 = 0.25$, $J_{n,ss}^1/(EH) = 2.0e^{-6}$, $J_{n,ss}^2 = J_{n,ss}^1$, and $h/H = 0.1$. The mode II cohesive is identical to the corresponding mode I cohesive law.

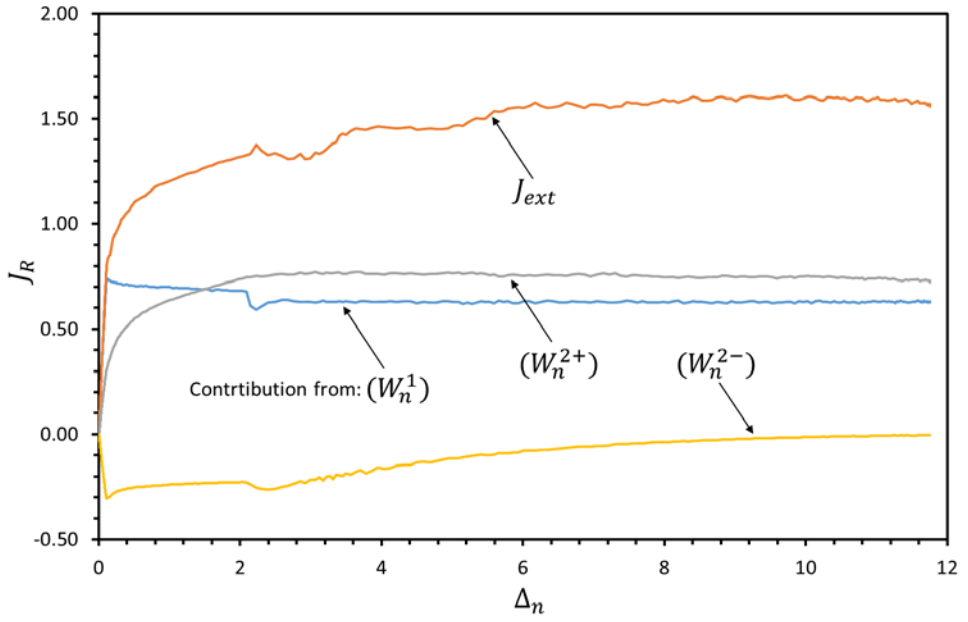

Figure 20 Contribution from the normal work of tractions: from the primary crack, the left(-) and right (+) crack tips of the secondary crack. The parameters are given in Figure 19.

The DACOMAT project has received funding from the European Union's Horizon 2020 research and innovation programme under GA No. 761072

Figure 21 is similar to Figure 20 but the contribution form the shear tractions of the primary crack (W_t^1) and from the left crack tip (W_t^{2-}) and right crack tip (W_t^{2+}) of the secondary crack are plotted. First, it can be seen that the contribution from the shear tractions is small but not zero e.g. although the applied load corresponds to pure mode I, due to the asymmetry both cracks experience also a shear opening. Similar to Figure 20, the small negative contribution from the left crack tip of the secondary should be noticed.

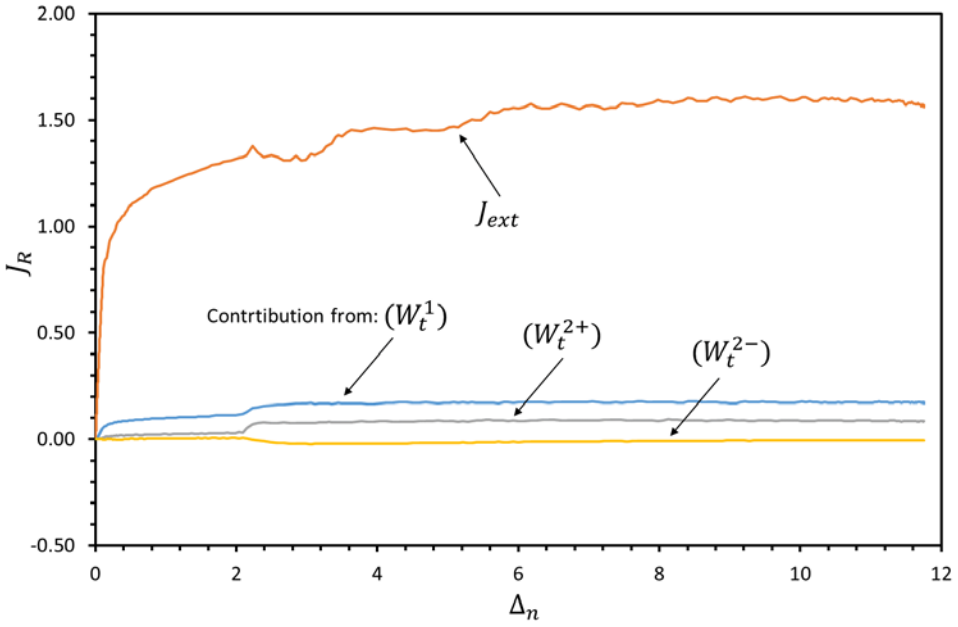

Figure 21 Contribution from the shear (tangential) work of tractions: from the primary crack, the left (-) and right (+) crack tips of the secondary crack. The parameters are given in Figure 19.

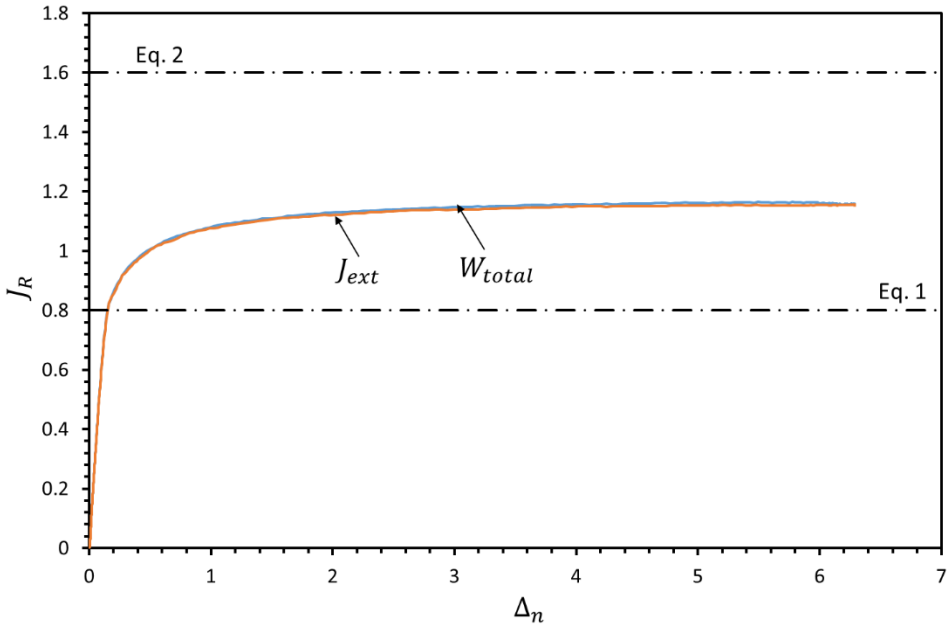

Figure 22 Fracture resistance as a function of the normal end-opening (of both the primary and secondary crack). J_{ext} is calculated from Eq. 11. W_{total} is the work of all tractions. $\hat{\sigma}_n^1/E = 2.5e^{-4}$, $\hat{\sigma}_n^2/\hat{\sigma}_n^1 = 0.50$, $J_{n,ss}^1/(EH) = 2.0e^{-6}$, $J_{n,ss}^2 = J_{n,ss}^1$, and $h/H = 0.1$. The mode II cohesive is identical to the corresponding mode I cohesive law.

The DACOMAT project has received funding from the European Union's Horizon 2020 research and innovation programme under GA No. 761072

Figure 22 is similar to Figure 19 but the peak traction of the primary crack has a higher value and $\hat{\sigma}_n^2/\hat{\sigma}_n^1$ is equal to 0.50. For this set of cohesive law parameters, the steady-state fracture resistance is significantly lower than the upper limit (Eq. 2). This is due to the negative contribution from the left crack tip as can be seen in Figure 23, combined with the reduced contribution from the right crack tip (compare with Figure 19).

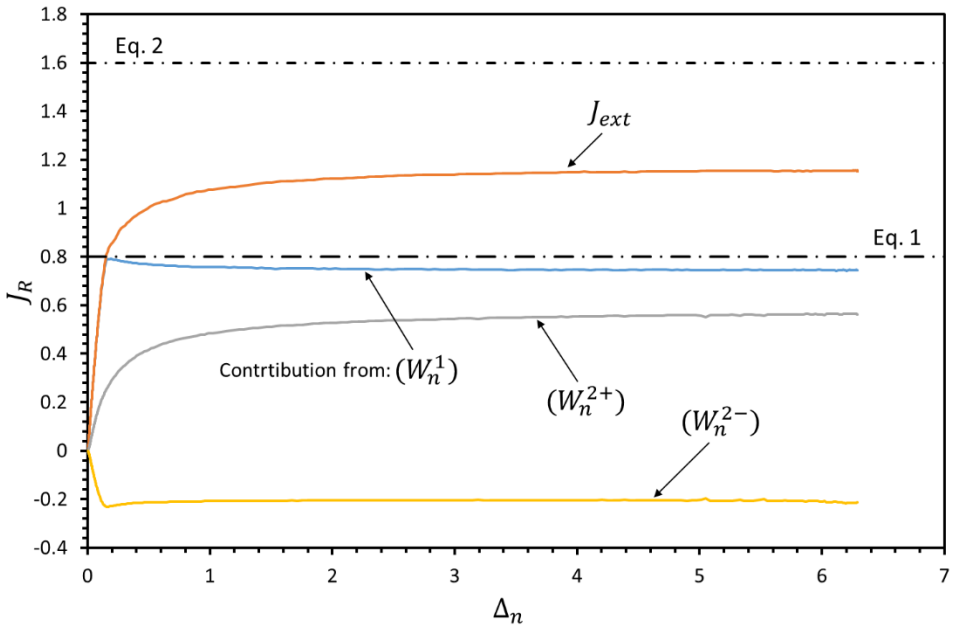

Figure 23 Contribution from the normal work of tractions: from the primary crack, the left(-) and right (+) crack tips of the secondary crack. The parameters are given in Figure 22.

Based on these results (including the deformation shapes of the model), and several other simulations that are not included, it can be stated that the analytical model correctly predicts a negative contribution from the left crack tip when it is open.

The DACOMAT project has received funding from the European Union's Horizon 2020 research and innovation programme under GA No. 761072

5.3 Bi-linear softening behaviour

In this Section the cohesive law of Section 3.2 will be used e.g. a cohesive law with bi-linear softening for mode I and mode II to separate the crack tip fracture process zone from the bridging zone. As it is clear from Eqs. 6-10, the number of parameters is large, and the result is in some cases rather complicated graphs.

Figure 24 shows the effect of the crack tip peak tractions ratio $\hat{\sigma}_n^{2,c}/\hat{\sigma}_n^{1,c}$ on the steady-state fracture resistance for five $\hat{\sigma}_n^{1,c}/E$ ratios when $h/H = 0.06$. The results of this graph can be compared with the results of Figure 9 although it should be noted that $J_{n,ss}^1/(EH)$ varies between the two graphs. It can be seen that as $\hat{\sigma}_n^{1,c}/E$ increases, $J_{R,ss}$ approaches the upper limit of fracture resistance but this happens at lower $\hat{\sigma}_n^{2,c}/\hat{\sigma}_n^{1,c}$ values. In all cases, the obtained steady-state fracture resistance values are close to the upper limit (Eq. 2) of the case presented in Figure 9. This difference is due to the different $J_{n,ss}^1/(EH)$ values, as mentioned above.

Figure 25 shows a plot similar to that in Figure 24, but the distance between the two cracks is larger ($h/H = 0.1$). The same trends as in Figure 24 can be observed, but in this case the range of $\hat{\sigma}_n^{2,c}/\hat{\sigma}_n^{1,c}$ ratios that provide a maximum increase to the steady-state fracture resistance is smaller. A significant drop in the steady-state fracture resistance can be seen when $\hat{\sigma}_n^{2,c}/\hat{\sigma}_n^{1,c}$ is small.

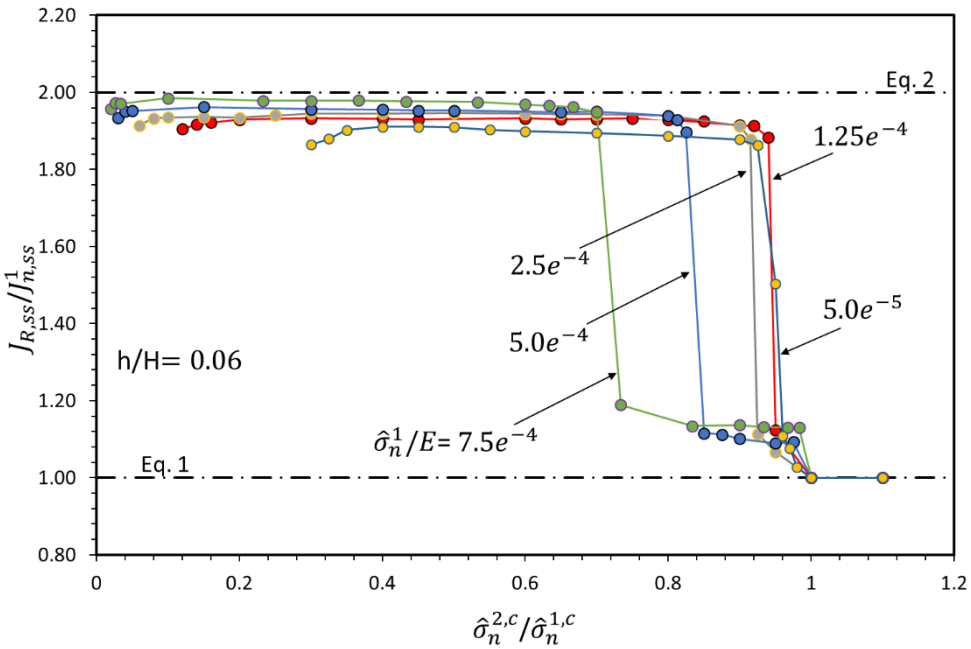

Figure 24 Steady-state fracture resistance, $J_{R,ss}$, as a function of the normal peak traction of the secondary crack, $\hat{\sigma}_n^{2,c}$, for five different $\hat{\sigma}_n^{1,c}/E$ ratios. The distance between the two cracks is $h/H = 0.06$. $J_{n,ss}^{1,c} = J_{n,ss}^{2,c}$, $J_{n,ss}^{1,b} = J_{n,ss}^{2,b}$, $J_{n,ss}^{1,b} = 3J_{n,ss}^{1,c}$, $\hat{\sigma}_n^{1,b}/\hat{\sigma}_n^{1,c} = 0.1$, $\hat{\sigma}_n^{2,b} = \hat{\sigma}_n^{1,b}$. The mode II cohesive law is identical to the mode I cohesive law for both cracks.

The DACOMAT project has received funding from the European Union's Horizon 2020 research and innovation programme under GA No. 761072

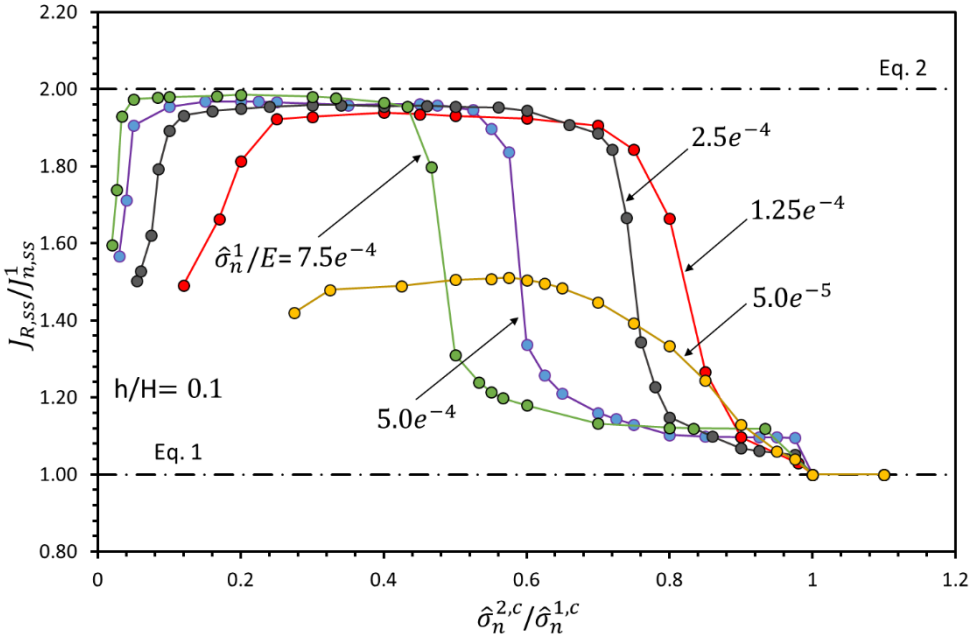

Figure 25 Steady-state fracture resistance, $J_{R,SS}$, as a function of the normal peak traction of the secondary crack, $\hat{\sigma}_n^{2,c}$, for five different $\hat{\sigma}_n^{1,c}/E$ ratios. The cohesive law parameters are identical to those of Figure 24. The difference is that the distance between the two cracks is $h/H = 0.1$.

In Figure 26 the effect of the ratio of the peak traction for the bridging region and the peak traction of the crack tip region. ($\hat{\sigma}_n^{1,b}/\hat{\sigma}_n^{1,c}$) is examined. For the definition of these peak tractions see Figure 13. The aim of Figure 26 it is to investigate if the steady-state fracture resistance can be increased by increasing the peak traction of the bridging zone of the primary crack for the cohesive law parameters that give low steady-fracture resistance in Figure 25. In Figure 25, for $\hat{\sigma}_n^{1,c}/E = 2.5e^{-4}$ and $\hat{\sigma}_n^{2,c}/\hat{\sigma}_n^{1,c} = 0.8$, the steady-state fracture resistance is less than $1.2\, J_{n,ss}^1$. A variation in the normal peak traction of the bridging zone of the primary crack, $\hat{\sigma}_n^{1,b}$, does not result in any significant change in the steady-state fracture resistance. A decrease of the normal peak traction of the bridging zone of the secondary crack, $\hat{\sigma}_n^{2,b}$, results in a minor increase of by $J_{R,ss}$..

In Figure 27 the effect of increasing the fracture energy, from fibre bridging, of the secondary crack is examined for $\hat{\sigma}_n^{1,c}/E = 7.5e^{-4}$ and two particular cohesive laws parameters. One set gives a steady-state fracture resistance close to the upper limit and one closer to the lower limit (see Figure 25). Increasing or decreasing $J_{n,ss}^{2,b}$ do not influence the steady-state fracture resistance for the set that is closer to the lower limit. For the other set, increasing $J_{n,ss}^{2,b}$ results in an increase of the state fracture resistance up to a certain point. Further increase of $J_{n,ss}^{2,b}$ actually results in a decrease of $J_{R,ss}$.

Figure 28 plots the same data as Figure 27 with the difference that the steady-state fracture resistance is shown as a function of the ratio of the fracture energies of the bridging zones of the secondary and the primary crack. This is to show that $J_{n,ss}^{2,b}$ has been increased several times.

Figure 29 is similar to Figure 27 but with two different sets of cohesive law parameters and $\hat{\sigma}_n^{1,c}/E = 2.5e^{-4}$ (see also Figure 25) in order to show that the conclusions drawn from Figure 27 are generic. An increase of the bridging zone fracture energy of the secondary crack does not have a positive effect on

The DACOMAT project has received funding from the European Union's Horizon 2020 research and innovation programme under GA No. 761072

the overall steady-state fracture resistance except in few cases and only when $J^1_{n,ss}/(EH)$ is relatively small.

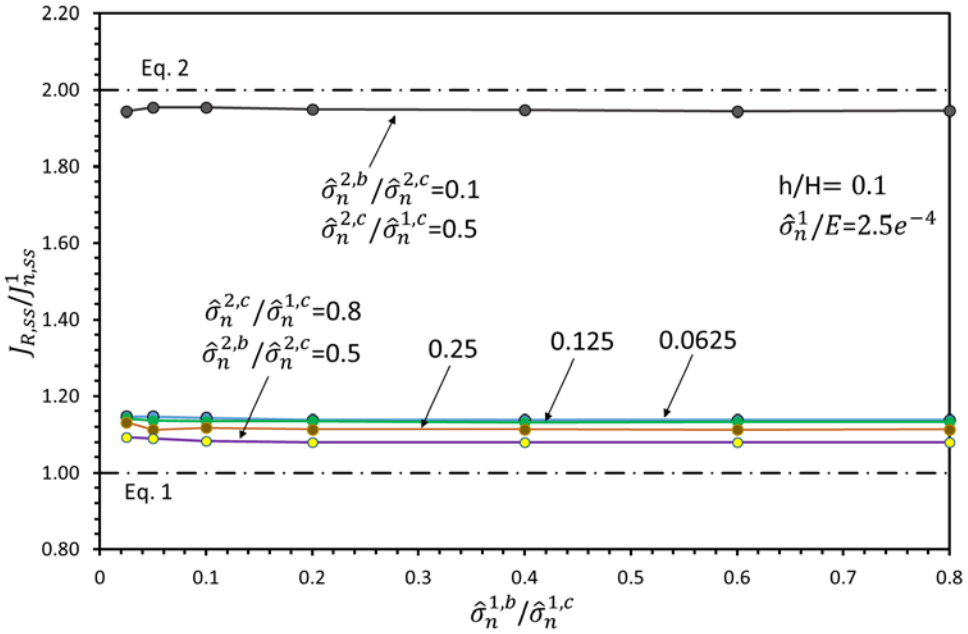

Figure 26 Steady-state fracture resistance, $J_{R,ss}$, as a function of the ratio of the normal crack tip peak traction with the normal bridging peak traction of the primary crack, $\hat{\sigma}_n^{1,b}/\hat{\sigma}_n^{1,c}$ for two $\hat{\sigma}_n^{2,c}/\hat{\sigma}_n^{1,c}$ ratios and five $\hat{\sigma}_n^{2,b}/\hat{\sigma}_n^{2,c}$ratios. $J^{1,c}_{n,ss} = J^{2,c}_{n,ss}, J^{1,b}_{n,ss} = J^{2,b}_{n,ss}, J^{1,b}_{n,ss} = 3\,J^{1,c}_{n,ss}$. The mode II cohesive laws are identical to the mode I cohesive laws for both the primary and secondary cracks.

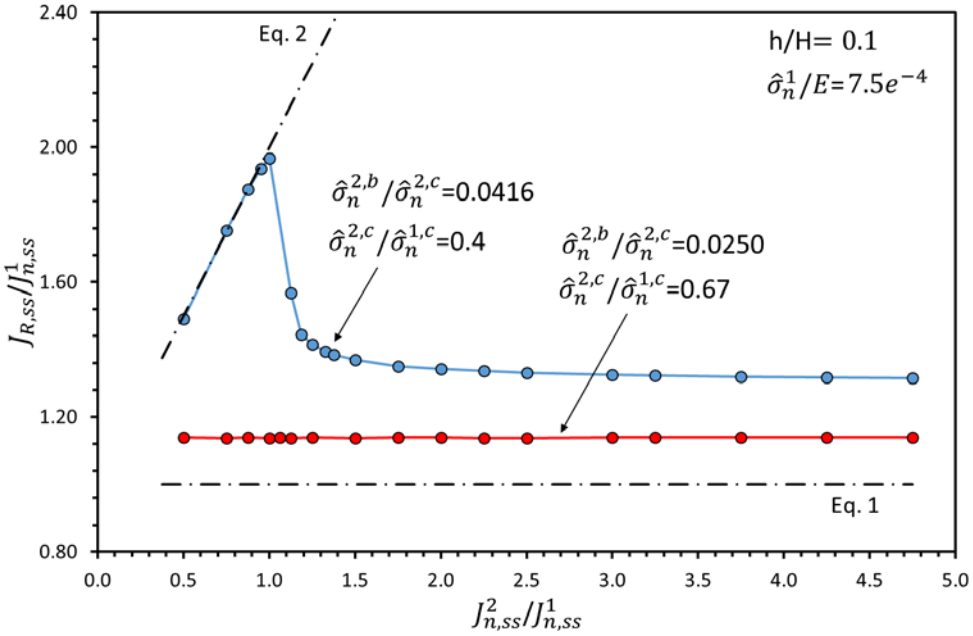

Figure 27 Steady-state fracture resistance, $J_{R,ss}$, as a function of the ratio of the fracture energy of the secondary crack with the fracture energy of the primary crack for two ratios of the normal crack tip tractions. $J^{1,c}_{n,ss} = J^{2,c}_{n,ss}, J^{1,b}_{n,ss} = 3J^{1,b}_{n,ss}, \hat{\sigma}_n^{1,b}/\hat{\sigma}_n^{1,c} = 0.0167$.

The DACOMAT project has received funding from the European Union's Horizon 2020 research and innovation programme under GA No. 761072

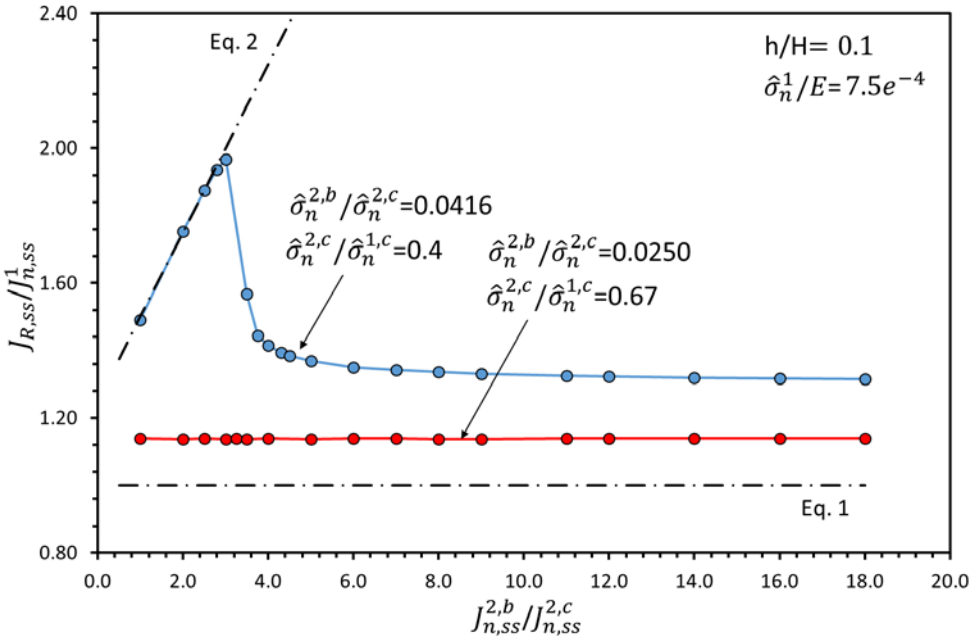

Figure 28 The results of Figure 27 are replotted with a change in the x-axis, which is the ratio of the bridging fracture energy over the crack tip fracture energy of the secondary crack.

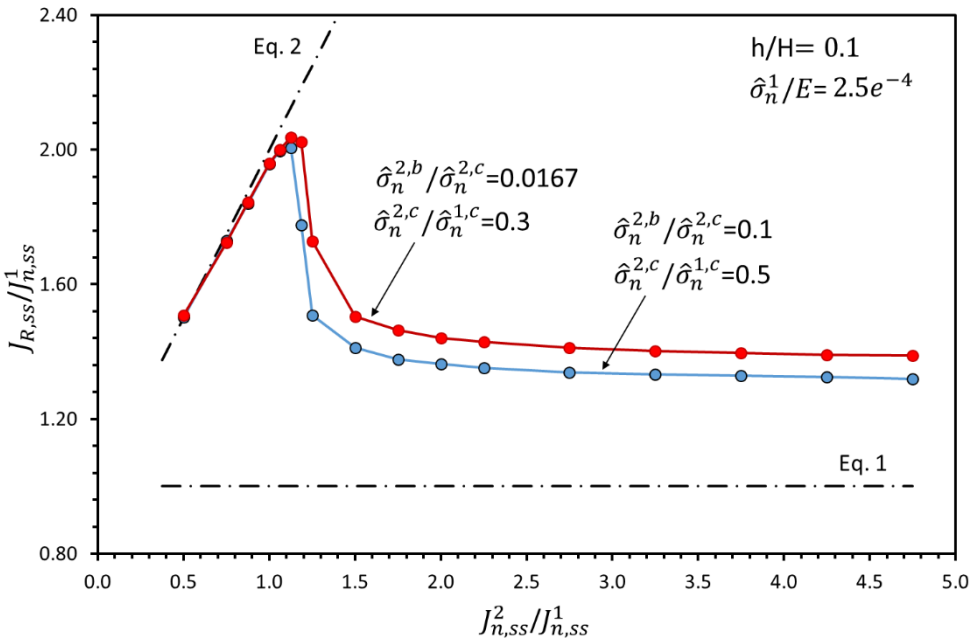

Figure 29 Steady-state fracture resistance, $J_{R,ss}$, as a function of the ratio of the fracture energy of the secondary crack with the fracture energy of the primary crack for two ratios of the normal crack tip tractions. $J_{n,ss}^{1,c} = J_{n,ss}^{2,c}$, $J_{n,ss}^{1,b} = 3J_{n,ss}^{1,b}$, $\hat{\sigma}_n^{1,b}/\hat{\sigma}_n^{1,c} = 0.05$.

The DACOMAT project has received funding from the European Union's Horizon 2020 research and innovation programme under GA No. 761072

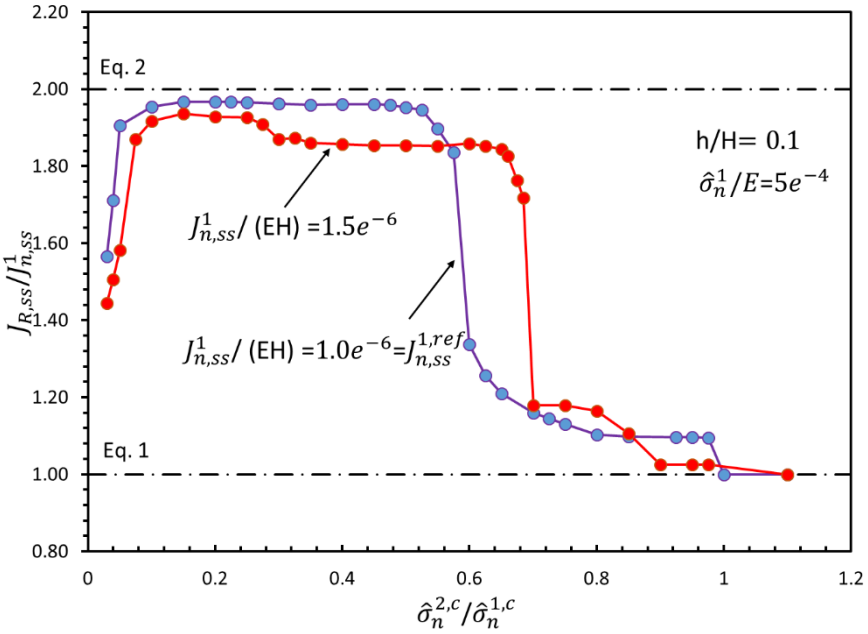

Figure 30 Steady-state fracture resistance, $J_{R,ss}$, as function of the normal peak traction ratio $\hat{\sigma}_n^{2,c}/\hat{\sigma}_n^{1,c}$. $\hat{\sigma}_n^{1,b}/\hat{\sigma}_n^{1,c} = 0.025$, $\hat{\sigma}_n^{2,b} = \hat{\sigma}_n^{1,b}$, $J_{n,ss}^{1,c} = J_{n,ss}^{2,c}$, and for each crack $J_{n,ss}^{1,b} = J_{n,ss}^{2,b}$.

Figure 30 shows the effect of increasing the fracture energy of the primary crack. Both the primary and secondary crack have the same crack tip fracture energy. Thus, the increase is due to the bridging zone fracture energy. For both cases, the secondary and primary cracks have the same bridging zone fracture energy. The mechanisms of increasing the steady-state fracture energy is less effective when the fracture energy of the primary crack increases.

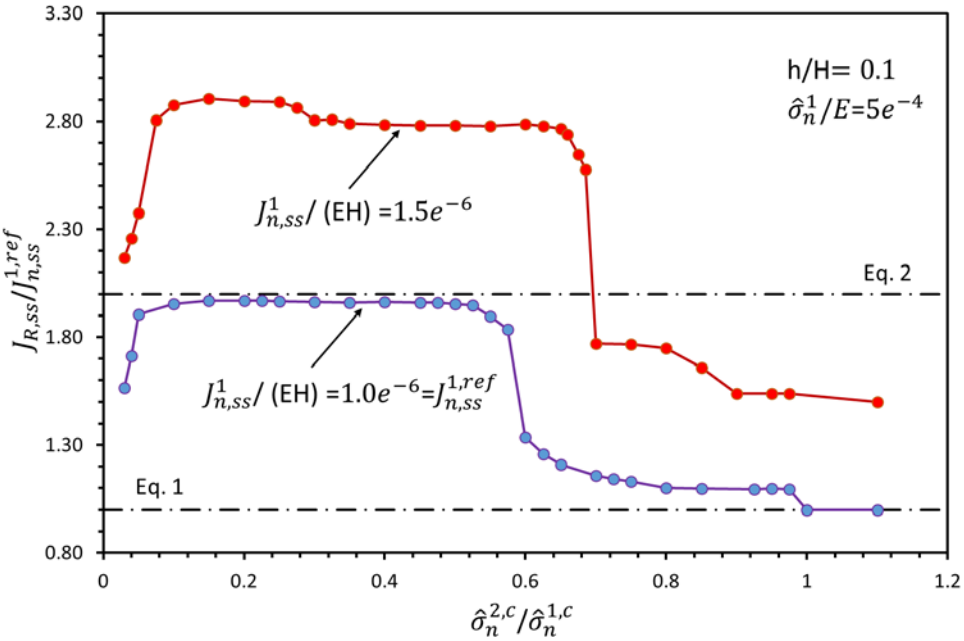

Figure 31 Replot of Figure 30 but the steady state fracture resistance is normalised with $J_{n,ss}^{1,ref}$ which is equal to the case $J_{n,ss}^1/(EH) = 1.0e^{-6}$.

The DACOMAT project has received funding from the European Union's Horizon 2020 research and innovation programme under GA No. 761072

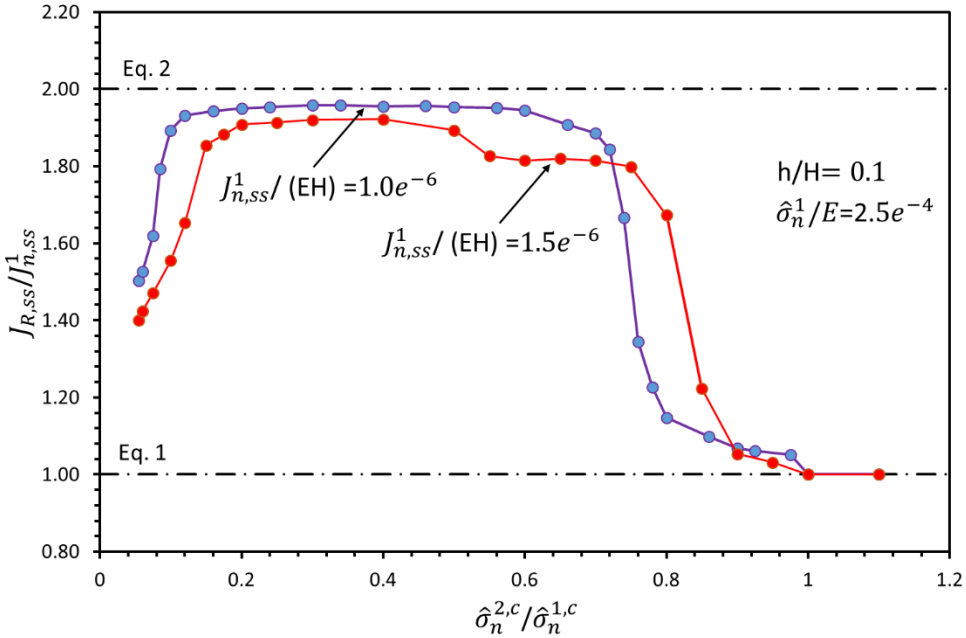

Figure 32 Similar plot to Figure 30 but for $\hat{\sigma}^1_n/E = 2.5e^{-4}$.

Assuming that the fracture energy of the primary crack is increased from $J^1_{n,ss}/(EH) = 1.0e^{-6}$ to $J^1_{n,ss}/(EH) = 1.5e^{-6}$. Then, Figure 30 can be replotted in Figure 31 where the steady-state fracture resistance is normalised with $J^1_{n,ss}/(EH) = 1.0e^{-6} = J^{1,ref}_{n,ss}$. Then, although the multiple cracks mechanisms are less pronounced, the absolute steady-state fracture resistance is significantly higher.

Figure 32 is similar to Figure 30 but for other $\hat{\sigma}^1_n/E$ values. The same conclusions as in Figure 30 can be drawn. The same trend were found also in other simulations, thus the results of Figure 30 and Figure 32 are generic.

The DACOMAT project has received funding from the European Union's Horizon 2020 research and innovation programme under GA No. 761072

6. Conclusions

The effect of cohesive law parameters that promote the formation of secondary delaminations / cracks with maximum increase in steady-state fracture resistance was investigated. For this purpose, two cohesive laws were defined and programmed as user material subroutines for the finite element software Abaqus.

Considering the cohesive laws with bi-linear softening behaviour (more relevant for the DACOMAT project) where the crack tip fracture energy is separated from the fracture energy of the bridging zone the following recommendations can be given.

- The fracture energy of the primary crack should be increased as much as possible. The secondary front is less effective in this case but the absolute increase in steady-state fracture resistance is higher.
- Once the steady-state fracture resistance of the primary crack is maximised, the effectiveness of the secondary crack can be optimised by tailoring its crack tip peak traction with respect to the crack tip peak traction of the primary crack. The peak tractions of the bridging zones have a minor effect.
- The peak traction of the primary crack must be as high as possible.

The DACOMAT project has received funding from the European Union's Horizon 2020 research and innovation programme under GA No. 761072

References

Bao, J. G., Ho, S., Fan, B., & Suo, Z. (1992). The role of material orthotropy in fracture specimens for composites. *International Journal of Solids and Structures, 29*, 1105-1116.

Goutianos, S., & Sørensen, B. F. (2016). Fracture resistance enhancement of layered structures by multiple cracks. *Engineering Fracture Mechanics*, 92-108.

Kusano., Y., Sørensen, B. F., & Andersen, T. L. (2013). Adhesion improvement of glass-fibre-reinforced polyester composites by gliding arc discharge treatment. *The Journal of Adhesion, 89*, 433-459.

Rask, M., & Sørensen, B. F. (2012). Determination of the J integral for laminated double cantilever beam specimens: The curvature approach. *Engineering Fracture Mechanics, 96*, 37-48.

Rice, J. (1968). A path independent integral and the approximate analysis of strain concentrations by notches and cracks. *Journal of Applied Mechanics, 35*, 379-386.

Sørensen, B. F., & Jacobsen, T. K. (2000). Characterizing delamination of fibre composites by mixed mode cohesive laws. *Composites Science and Technology, 69*, 445-456.

Sørensen, B. F., Jørgensen, K., Jacobsen, T. K., & Østergaard., R. C. (2006). DCB-specimen loaded with uneven bending moments. *International Journal of Fracture, 141*, 164-176.

The DACOMAT project has received funding from the European Union's Horizon 2020 research and innovation programme under GA No. 761072